Transferrin receptor (TfR) trafficking determines brain uptake of TfR antibody affinity variants

Nga Bien-Ly,[1] Y. Joy Yu,[1] Daniela Bumbaca,[2] Justin Elstrott,[3] C. Andrew Boswell,[2] Yin Zhang,[4] Wilman Luk,[5] Yanmei Lu,[5] Mark S. Dennis,[4] Robby M. Weimer,[1,3] Inhee Chung,[6] and Ryan J. Watts[1]

[1]Department of Neuroscience, [2]Development Sciences, [3]Biomedical Imaging Group, [4]Antibody Engineering Group, [5]Biochemical and Cellular Pharmacology Group, and [6]Molecular Oncology Group, Genentech Inc., South San Francisco, CA 94080

The Journal of Experimental Medicine

Antibodies to transferrin receptor (TfR) have potential use for therapeutic entry into the brain. We have shown that bispecific antibodies against TfR and β-secretase (BACE1 [β-amyloid cleaving enzyme-1]) traverse the blood–brain barrier (BBB) and effectively reduce brain amyloid β levels. We found that optimizing anti-TfR affinity improves brain exposure and BACE1 inhibition. Here we probe the cellular basis of this improvement and explore whether TfR antibody affinity alters the intracellular trafficking of TfR. Comparing high- and low-affinity TfR bispecific antibodies in vivo, we found that high-affinity binding to TfR caused a dose-dependent reduction of brain TfR levels. In vitro live imaging and colocalization experiments revealed that high-affinity TfR bispecific antibodies facilitated the trafficking of TfR to lysosomes and thus induced the degradation of TfR, an observation which was further confirmed in vivo. Importantly, high-affinity anti-TfR dosing induced reductions in brain TfR levels, which significantly decreased brain exposure to a second dose of low-affinity anti-TfR bispecific. Thus, high-affinity anti-TfR alters TfR trafficking, which dramatically impacts the capacity for TfR to mediate BBB transcytosis.

CORRESPONDENCE
Ryan J. Watts:
rwatts@gene.com
OR
Inhee Chung:
chung.inhee@gene.com

Abbreviations used: BBB, blood–brain barrier; QD, quantum dot; Tf, transferrin; TfR, Tf receptor; TIRFM, total internal reflection fluorescence microscopy.

The blood–brain barrier (BBB) limits the passage of most macromolecules from the periphery into the brain. However, several essential nutrients and carrier proteins are thought to cross the BBB via receptors expressed on brain endothelial cells through a process known as receptor-mediated transcytosis (Rubin and Staddon, 1999; Predescu et al., 2007). Transferrin (Tf) receptor (TfR), a type II transmembrane protein highly expressed on brain endothelial cells (Jefferies et al., 1984; Kissel et al., 1998), has been proposed to undergo transcytosis at the BBB to allow entry of iron-bound Tf by constitutive endocytosis (Fishman et al., 1987; Roberts et al., 1993). Although it is known that iron dissociates from Tf in acidified endosomes and the Tf–TfR complex recycles back to the plasma membrane (Dautry-Varsat et al., 1983; Sheff et al., 2002; Traer et al., 2007), the exact route of receptor-mediated transcytosis of Tf–TfR is not well understood at the BBB.

TfR has been actively explored to deliver protein therapeutics to the brain (Jones and Shusta, 2007; Yu and Watts, 2013), although an understanding of precise cellular mechanisms associated with TfR trafficking at the BBB remains unclear. Indeed, delivery of drug-Tf conjugates and TfR antibody conjugates have had some success (Dufès et al., 2013; Yu and Watts, 2013), though many limitations have also surfaced, including evidence that high-affinity TfR antibodies remain trapped within brain vasculature (Moos and Morgan, 2001; Gosk et al., 2004; Paris-Robidas et al., 2011; Yu et al., 2011; Manich et al., 2013). We have previously shown that in the context of both anti-TfR and bispecific anti-TfR/BACE1 (β-amyloid cleaving enzyme-1), greater brain exposure is achieved as the affinity for TfR is reduced (Yu et al., 2011; Couch et al., 2013). We proposed that lower affinity enhances uptake into brain by facilitating dissociation from TfR (Yu et al., 2011). We also recently reported that affinity and

The Rockefeller University Press $30.00
J. Exp. Med. 2014 Vol. 211 No. 2 233-244
www.jem.org/cgi/doi/10.1084/jem.20131660

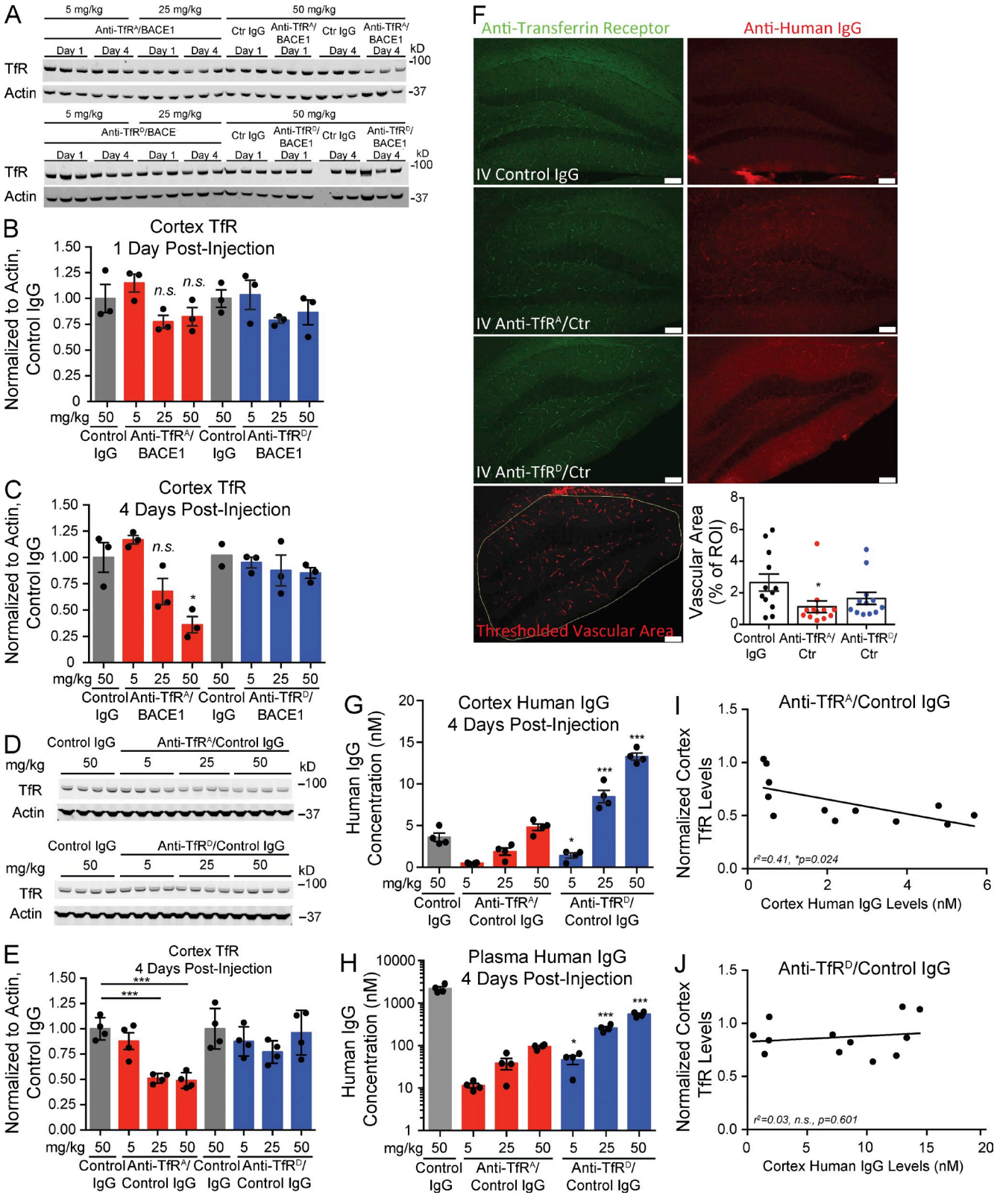

Figure 1. High-affinity anti-TfR bispecific variants reduce cortical TfR levels. (A–C) Mice were i.v. injected with various doses of anti-TfR bispecific high- and low-affinity variants, and cortical TfR levels were assessed by Western blot. Quantification of cortex TfR levels normalized to actin and control IgG–dosed animals at 1 and 4 d after dosing with anti-TfR/BACE1 bispecific affinity variants or a control (Ctr) IgG. One sample from the 4 d anti-TfR^D/BACE1 control IgG group did not produce a significant band (A, bottom); however, these same 4 d control IgG samples also appear in

effector function determine the safety profile of TfR therapeutic antibodies in vivo, thus further supporting low-affinity approaches and the need to better understand the underlying cell biology (Couch et al., 2013). Here, we hypothesized that TfR antibody affinity determines TfR trafficking fate and sought to study the cellular mechanisms underlying the robust differences between high and low anti-TfR affinity variants and TfR trafficking, as well as the impact of these strategies on brain uptake of biotherapeutics.

RESULTS

High-affinity binding to TfR drives cortical TfR degradation in vivo

To understand how anti-TfR affinity inversely impacts brain exposure to antibody, we first determined whether levels of TfR are affected by dosing of high- versus low-affinity TfR bispecific antibodies. Wild-type mice were given a single i.v. injection at one of three doses (5, 25, and 50 mg/kg) of high-affinity anti-TfR^A/BACE1 or low-affinity anti-TfR^D/BACE1, and TfR protein levels in the cortex were assessed at 1 and 4 d after injection by Western blot from brain homogenates. The bispecific variants share an identical non-Tf–TfR blocking epitope, and affinities were previously determined as ∼20 nM for anti-TfR^A/BACE1 and ∼600 nM for anti-TfR^D/BACE1 (Couch et al., 2013). A negative control group received an isotype control human IgG at the highest dose (50 mg/kg). Subtle reductions in cortical TfR levels were observed 1 d after dose with the 25- and 50-mg/kg doses of anti-TfR^A/BACE1 (Fig. 1, A and B); these trends were more pronounced at 4 d after dose. In fact, TfR levels were reduced >50% with 50 mg/kg anti-TfR^A/BACE1 at 4 d after dose (Fig. 1 C). No significant changes in TfR levels were observed with the low-affinity anti-TfR^D/BACE1 at any dose level or time point. To determine whether the anti-BACE1 arm of high-affinity anti-TfR^A/BACE1 bispecific contributes to the observed decreases in TfR protein levels in vivo, a control IgG arm was substituted for anti-BACE1. Mice were dosed with high-affinity anti-TfR^A/control IgG or low-affinity anti-TfR^D/control IgG. Similar to high-affinity anti-TfR^A/BACE1, the higher doses of anti-TfR^A/control IgG reduced the levels of cortical TfR when assessed at 4 d (Fig. 1, D and E). Importantly, low-affinity anti-TfR^D/control IgG did not decrease TfR at any dose level.

To determine the distribution of TfR loss, mouse hippocampus was stained with a noncompeting anti-TfR antibody 4 d after dose (50 mg/kg), and quantitative analysis was conducted to localize TfR reductions (Fig. 1 F). When images were analyzed specifically for vascular TfR, only anti-TfR^A/control IgG showed a significant reduction. We also observed a qualitative decrease in parenchymal TfR staining with anti-TfR^A/control IgG dosing, reflecting possible TfR reductions in neurons. Detection of injected human IgG revealed increased staining for both TfR bispecific antibodies, with a broader parenchymal distribution observed for anti-TfR^D/control IgG. Consistent with a previous study (Couch et al., 2013), cortical antibody concentrations of anti-TfR^A/control IgG were significantly lower than anti-TfR^D/control IgG at all three doses (Fig. 1 G), again demonstrating improved brain exposure with reduced affinity. Plasma antibody concentrations for both anti-TfR affinity variants were lower than for control IgG as the result of TfR-mediated and affinity-driven clearance (Fig. 1 H). We found a clear inverse correlation between cortical TfR levels and brain antibody concentrations for anti-TfR^A/control IgG ($R^2 = 0.41$, $P = 0.024$) but not with anti-TfR^D/control IgG ($R^2 = 0.03$, $P = 0.601$; Fig. 1, I and J). These findings suggest that high-affinity bispecific antibodies to TfR, regardless of the therapeutic target arm, cause dose-dependent decreases in cortical TfR levels, with a quantifiable reduction observed in vessels. We hypothesize that higher antibody affinity alters the endocytic sorting route of TfR toward a degradative pathway in vivo, consequently impacting both transcytosis capacity and antibody brain exposure compared with lower-affinity TfR binding (Fig. 2 A).

Greater degradation of high-affinity TfR bispecific in brain as shown by ^{111}In accumulation

Having seen that TfR is degraded after high-affinity dosing, we next determined the fate of the anti-TfR bispecifics by coinjecting a trace dose of anti-TfR^A/control IgG, anti-TfR^D/control, or control IgG, each labeled with [^{111}In]DOTA or ^{125}I. The coinjection of radioiodinated antibody and the radiometal ^{111}In enables the measurement of relative rates of degradation between the anti-TfR affinity variants because of the unique residualizing characteristic of [^{111}In]DOTA upon antibody degradation at targeted tissues (Boswell et al., 2012). Plasma pharmacokinetic measurements of dose-normalized radioactivity for TfR^A bispecific were threefold lower than TfR^D bispecific or control IgG, and no differences were observed between ^{111}In and ^{125}I for all three antibodies (Fig. 2 B). Brain radioactivity determined at all time points revealed

the top blot. (D and E) Western blot of cortical TfR levels after injection with anti-TfR/control IgG bispecific variants at 4 d after dosing. Scatter points indicate individual mice sampled in each Western blot and data panel (n = 3–4 mice per group; except in C, n = 2 for the second control IgG group). (F) Immunohistochemistry for TfR 4 d after injection with anti-TfR/control IgG bispecific variants at 50 mg/kg and quantitative analysis of TfR-positive hippocampal vascular area. n = 4 mice were sampled per group, and three stained sections per mouse were quantified. Rabbit anti-TfR detects a different TfR epitope than the injected anti-TfR bispecific. Anti–human IgG reveals antibody distribution in the hippocampus. IV, i.v.; ROI, region of interest. Bars, 100 µm. (G and H) Total cortex (G) and plasma (H) human IgG antibody levels assessed by ELISA. (I and J) Scatter plot and correlation analysis of cortical TfR levels (from E) plotted against brain pharmacokinetics at 4 d after injection (from G) for all dosages of each bispecific (n = 12 in each scatter plot). Bar graphs show means of each group, and error bars are ± SEM; p-values were obtained by Student's t test versus control IgG groups, except in G and H where p-values compare corresponding doses of anti-TfR^A/control IgG: *, $P < 0.05$; ***, $P \leq 0.001$.

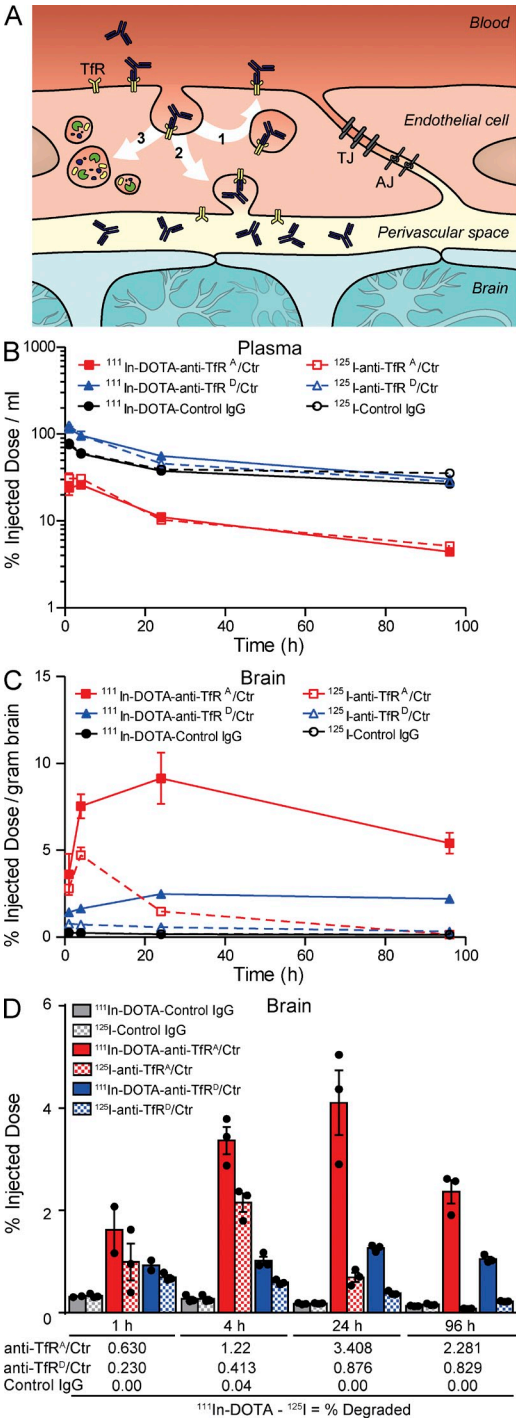

Figure 2. Greater degradation of high-affinity TfR^A bispecific as shown by ^{111}In accumulation in brain. (A) Schematic illustrating three potential endocytic sorting routes that anti-TfR bispecifics may take within endothelial cells at the BBB. Upon receptor binding, (1) anti-TfR bispecifics may be recycled to the luminal side (blood), (2) transcytosed to the parenchyma (brain), or (3) sorted to the lysosome for degradation. (B–D) Greater retention of [^{111}In]DOTA-anti-TfR^A/control (Ctr) IgG high-affinity variant in vivo. (B) Plasma pharmacokinetics of anti-TfR^A/control, anti-TfR^D/control, and control IgG labeled with either ^{111}In or ^{125}I assessed up to 96 h after dose. (C) Brain radioactivity levels over time were higher for anti-TfR^A/control compared with the other two antibodies. (D) ^{111}In signal exceeded and was sustained longer than ^{125}I for all antibodies in brain. The total uptake of anti-TfR^A/control in the brain was higher than that of anti-TfR^D/control and control IgG. The percentage of antibody degraded at each time point (shown below graph in D) was calculated by subtracting percent injected doses of ^{125}I signal from ^{111}In. All data are shown as mean ± SEM; n = 3 mice per antibody group and time point for all panels.

significantly greater levels of TfR^A bispecific, consistent with affinity-mediated uptake for trace dosing (Fig. 2 C). Levels of [^{111}In]anti-TfR^A bispecific were increased two- to threefold compared with [^{111}In]anti-TfR^D bispecific at 4 and 24 h, suggesting greater degradation of the higher affinity variant (Fig. 2 D, solid bars). Control IgG had little radioactive signal in the brain at all time points tested. By subtracting the levels of ^{125}I signal, we determined the total percentage of antibody degraded, which was consistently higher for the high-affinity TfR^A bispecific (Fig. 2 D). These in vivo results support the hypothesis that cellular TfR trafficking routes are altered from recycling to degradation because of high-affinity anti-TfR binding (Fig. 2 A), resulting in degradation of both TfR and anti-TfR.

High-affinity binding to TfR drives dose-dependent lysosomal degradation of TfR in vitro

To understand the subcellular mechanism of how antibody affinity affects TfR trafficking and stability, we characterized the expression of TfR in bEND.3 cells, an immortalized mouse brain endothelial cell line, after treatment with TfR^A or TfR^D bispecific antibodies. Incubation with high-affinity TfR^A bispecific resulted in a dose-dependent reduction in TfR protein levels by 24 h, whereas low-affinity TfR^D bispecific or control IgG did not reduce TfR levels at either 1 or 24 h (Fig. 3, A and B). A time course study revealed that TfR levels decreased 8 h after incubation with TfR^A bispecific and lasted up to 32 h (Fig. 3, C and D). Decreased TfR protein was not caused by transcriptional regulation of TfR expression, as there were no changes to TfR mRNA levels at 24 h, as assessed by quantitative PCR (not depicted).

We next determined whether TfR degradation was occurring through lysosomes by incubating bEND.3 cells with 1 µM TfR^A or TfR^D bispecifics for 24 h (the dose and time point with the most significant reduction in TfR protein levels) in the presence or absence of bafilomycin A1, an ATPase inhibitor which reduces lysosomal proteolytic enzyme activity. With bafilomycin A1 treatment, TfR^A bispecific no longer reduced TfR levels, which were similar to TfR^D bispecific or control IgG coincubation (Fig. 3 E). This finding suggests that anti-TfR treatment enhances the natural cellular degradation pathway for TfR and is consistent with recently published data reporting constitutive degradation of TfR in lysosomes (Matsui et al., 2011).

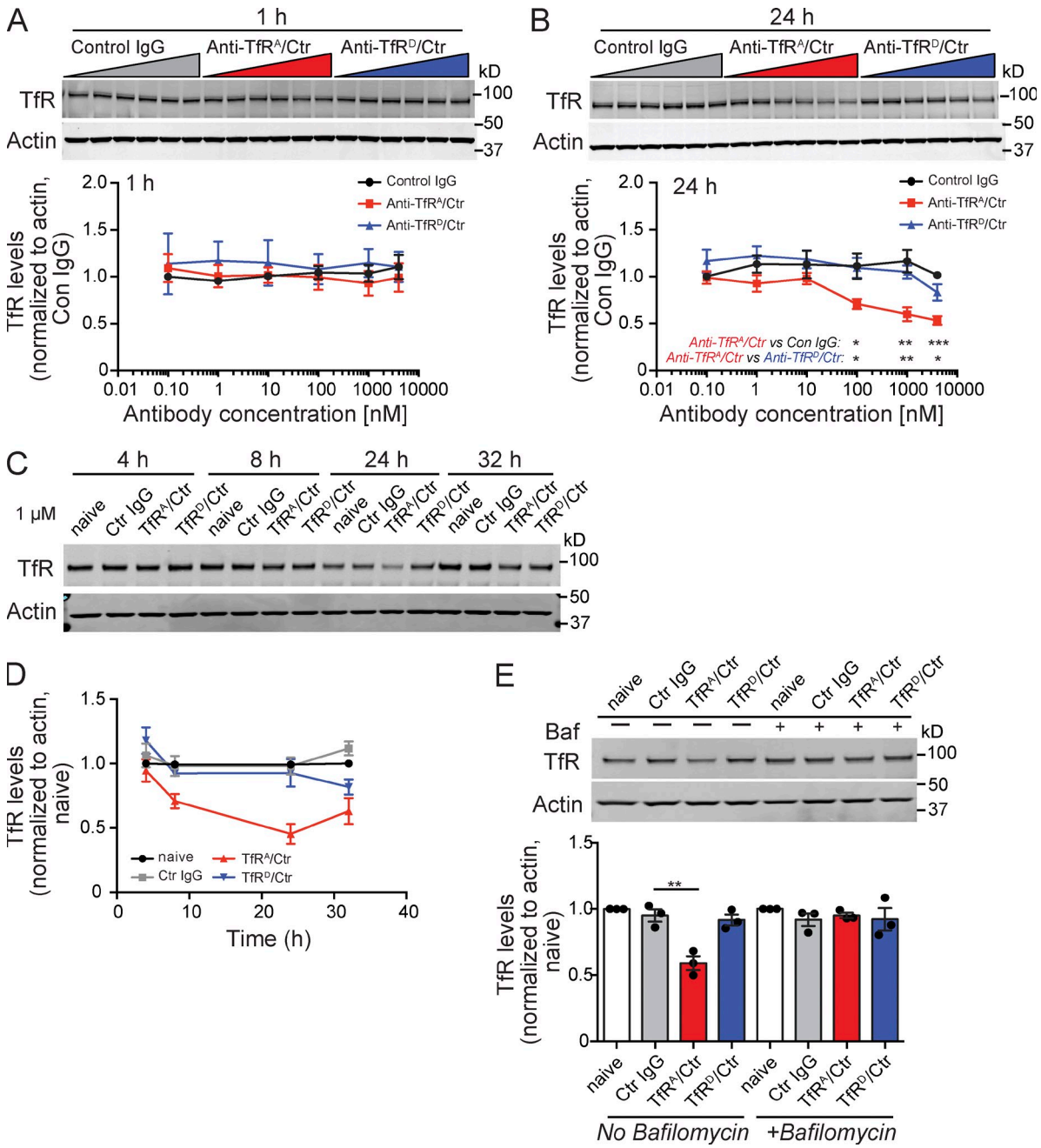

Figure 3. High-affinity anti-TfR^A bispecific causes dose-dependent lysosomal degradation of TfR in vitro. (A and B) Mouse brain endothelial cells (line bEND.3) were incubated with increasing levels of anti-TfR^A/control (Ctr), anti-TfR^D/control, or control IgG and collected at 1 (A) or 24 h (B) for Western blot analysis. Gel images and quantification are representative of three independent experiments. (C and D) Time course of TfR reductions after incubation with anti-TfR^A/control. Gel image and quantification of one experiment with triplicate wells are shown. All antibodies were used at 1 μM. (E) bEND.3 cells were incubated with the anti-TfR/control bispecific variants at 1 μM for 24 h in the absence or presence of 100 nM bafilomycin A1 (Baf), a lysosome protease inhibitor, and assessed by Western blot for TfR levels. Gel image and quantification are representative of three independent experiments, each performed in triplicate. All data are shown as mean ± SEM. P-values were assessed by Student's *t* test: *, $P < 0.05$; **, $P \leq 0.01$; ***, $P \leq 0.001$.

Enhanced trafficking of TfR to lysosomes upon treatment with high-affinity TfR bispecific antibodies

To further explore how anti-TfR affinity increases TfR degradation, we directly visualized the early trafficking dynamics and steady-state cellular distribution of TfR in bEND.3 cells after the addition of anti-TfR^A or anti-TfR^D bispecifics. Quantum dot (QD)–labeled anti–murine TfR Fab fragment (TfR-Fab:QD), recognizing a different epitope from the anti-TfR bispecifics, was used to track endogenous TfR at a single molecule level by total internal reflection fluorescence microscopy

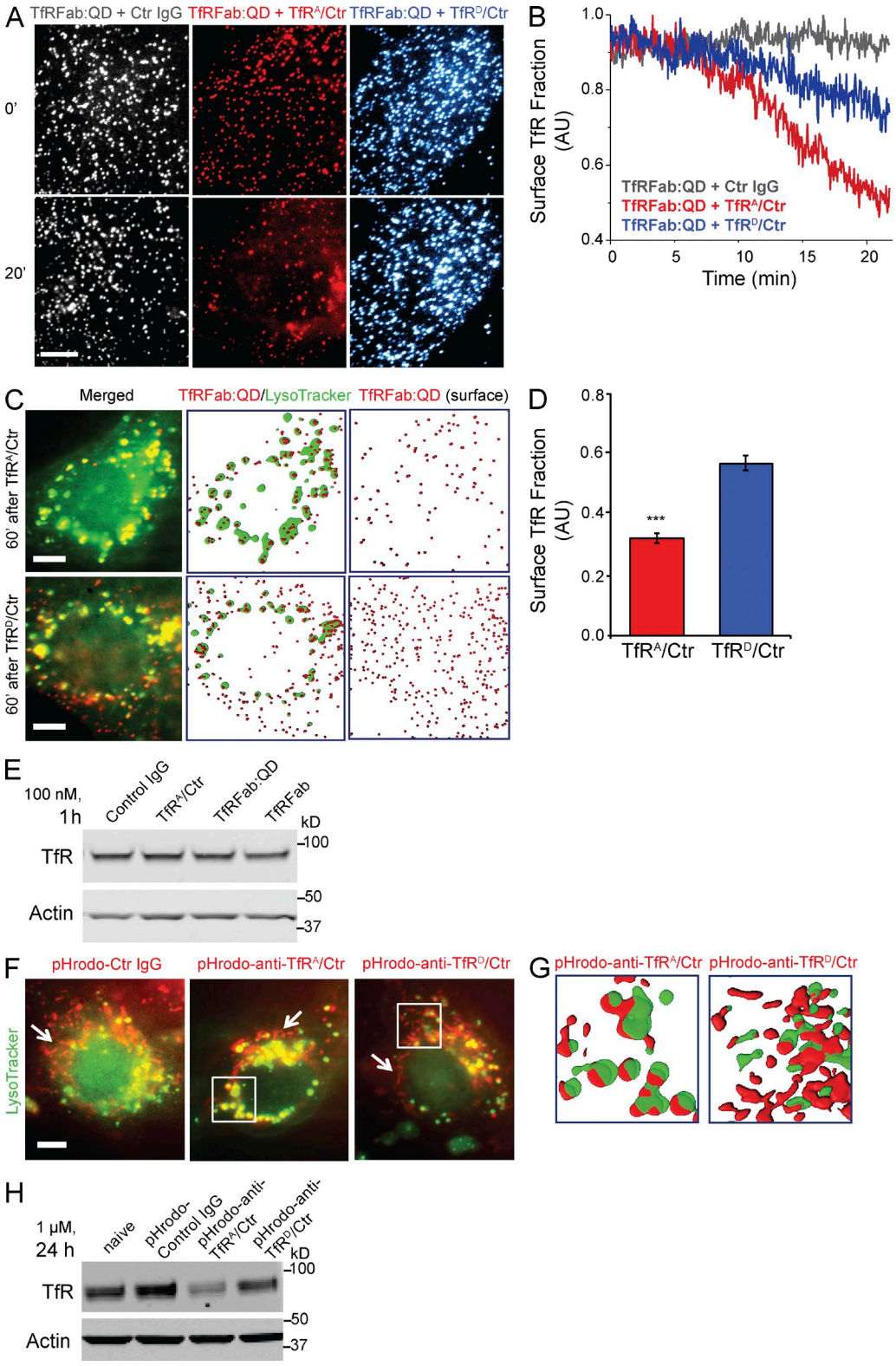

Figure 4. High-affinity TfR^A bispecific facilitates TfR trafficking to lysosomes. (A and B) Surface levels of TfR in bEND.3 cells were monitored by TIRFM using the QD (QD605)-conjugated anti-murine TfR Fab fragment (TfRFab:QD) of an antibody with a different epitope for TfR from the anti-TfR bispecifics. High- and low-affinity anti-TfR bispecifics were incubated at their respective IC_{50} concentrations to normalize for affinity differences. TfRFab:QD on basal membranes was tracked, imaged at 0 and 20 min (A), and quantified over 22 min with a 3-s laser illumination time interval (B). Images shown are pseudocolored. Quantification of the last 10 time points in B showed that TfR^A/control (Ctr) had 0.54 ± 0.01 surface TfR remaining relative to control IgG,

(TIRFM; Chung et al., 2010). We indeed observed differential dynamics of TfR internalization induced by anti-TfR bispecific affinity variants. When monitored continuously over the first 20 min after antibody addition, surface levels of TfRFab:QD (representing TfR) decreased significantly more with the addition of 20 nM high-affinity anti-TfR^A than with 600 nM low-affinity anti-TfR^D bispecific (Fig. 4, A and B). These antibody concentrations were chosen based on their respective affinities to normalize differences in TfR occupancy by anti-TfR bispecific on the cell surface at the start of the experiment and to allow for a relative comparison because of their large affinity differences.

The differential internalization of TfR by binding to antibodies with differing affinities does not necessarily imply that bound TfR undergoes different intracellular trafficking. Thus, we compared the steady-state distribution of bound TfR after incubation with anti-TfR^A or anti-TfR^D bispecific in live cells (Fig. 4 C). After 1-h coincubation with the anti-TfR bispecifics, we followed the movement of TfRFab:QD-labeled TfR relative to lysosomes (labeled by LysoTracker) by manipulating the depth of field. We observed more colocalization of TfRFab:QD in LysoTracker-positive compartments with TfR^A bispecific and found TfR more homogenously widespread within cells incubated with TfR^D bispecific. Additionally, the steady-state surface fraction of TfR with TfR^D bispecific was 44% greater than with TfR^A bispecific (Fig. 4 D). We verified that TfRFab:QD labeling of TfR under these experimental conditions did not down-regulate TfR levels (Fig. 4 E). Thus, these results clearly show that high-affinity anti-TfR^A bispecific not only increased TfR internalization, but also altered the trafficking and fate of the receptor by inducing more TfR movement toward lysosomes for degradation.

Because we observed the increased degradation of ^{111}In-labeled anti-TfR^A bispecific in vivo, we next examined whether TfR^A bispecific itself exhibited increased trafficking into lysosomes. Anti-TfR^A and anti-TfR^D bispecific were labeled with pHrodo, a low pH–sensitive fluorescent dye, and used to assess uptake into cells in the presence of LysoTracker. After 1 h of coincubation with LysoTracker, we found visibly more pHrodo–anti-TfR^A bispecific in LysoTracker-positive compartments compared with pHrodo–control IgG or pHrodo–anti-TfR^D bispecific (Fig. 4 F), both of which had more signal in tubular structures (Fig. 4, F [white arrows and boxed regions] and G), likely representing fast-sorting and recycling endosomes (Traer et al., 2007). Incubations were performed at the respective IC_{50} concentration for TfR^A bispecific (20 nM) and for TfR^D bispecific (600 nM), whereas the control IgG was used at 600 nM. Levels of TfR protein were assessed by Western blot upon 24 h of incubation with 1 µM pHrodo-labeled antibodies to exclude any effects caused by labeling. Again we observed that high-affinity TfR^A bispecific reduced TfR levels, demonstrating that pHrodo labeling did not alter TfR^A bispecific (Fig. 4 H).

We also performed immunocytochemistry for internalized anti-TfR bispecifics for colocalization with EEA1 (early endosomal-antigen-1) or LAMP1, a lysosomal marker. Although both anti-TfR^A and anti-TfR^D bispecifics colocalized with EEA1 at all time points tested (Fig. 5, A and D), more colocalization with LAMP1 was observed at 1 h for TfR^A bispecific than TfR^D bispecific when incubated at their respective IC_{50} concentrations (Fig. 5, B and E). As a positive control, fluorescently labeled Tf was tested in parallel to demonstrate TfR-specific endocytosis (Fig. 5, C and F). In the presence of TfR^A bispecific, we observed significantly more colocalization for TfR^A bispecific with LAMP1 by 2 h compared with TfR^D bispecific (Fig. 5 E), again supporting the hypothesis that anti-TfR binding promotes both antibody and TfR trafficking to the lysosome for degradation.

Recognizing the limitations of BBB in vitro models and our cellular system, we used in vivo two-photon microscopy to visualize subcortical vasculature and fluorescently labeled antibody to further understand the trafficking dynamics of TfR bispecific affinity variants in an intact BBB (Fig. 5, G and H). Our in vivo trafficking experiments revealed that pHrodo-labeled TfR^A bispecific accumulated into discreet puncta, presumably trapped within lysosomes of the endothelial cells along cortical brain vasculature in live mice (Fig. 5 H). No aggregates associated with the vasculature were observed with pHrodo-labeled TfR^D bispecific or control IgG.

Degradation of TfR limits antibody uptake into brain

TfR-dependent brain delivery approaches to cross the BBB likely rely heavily on the steady-state levels of available TfR

whereas TfR^D/control had 0.80 ± 0.01 surface TfR relative to control IgG (mean ± SEM). *n* = 8 cells analyzed for each condition. (C and D) Movement of TfRFab:QD after 1-h incubation with high- and low-affinity anti-TfR bispecific in the presence of LysoTracker. (C) TfRFab:QD was imaged relative to LysoTracker. The total internal reflection angle was adjusted to illuminate the inside and surface of the same cells in C. (D) Quantification of the remaining TfR fraction on the cell surface after 1-h incubation with anti-TfR bispecifics, TfR^A bispecific (0.32 ± 0.02, *n* = 74 cells analyzed) and TfR^D bispecific (0.57 ± 0.03, *n* = 40 cells analyzed). Mean ± SEM; ***, P < 0.0001 by one-tailed Student's *t* test for TfR^A bispecific versus TfR^D bispecific. (E) TfRFab:QD and TfRFab did not decrease TfR levels under TIRFM imaging conditions (1 h, 100 nM) as confirmed by Western blot (gel image is representative of three samples). (F) pHrodo-labeled anti-TfR bispecifics and control IgG were incubated for 1 h (at IC_{50} concentrations) in the presence of LysoTracker, and intracellular pools were imaged for extent of colocalization. More pHrodo–anti-TfR^A/control overlapped with LysoTracker-positive, perinuclear compartments, likely representing lysosomes, than pHrodo–anti-TfR^D/control or pHrodo–control IgG. Boxed perinuclear regions are shown to the right as rendered images (G) to compare the relative locations between pHrodo–anti-TfR^A/control and pHrodo–anti-TfR^D/control, with respect to LysoTracker. White arrows highlight tubular-shaped pools of endosomes containing significantly more pHrodo–anti-TfR^D/control or pHrodo–control IgG than pHrodo–anti-TfR^A/control. Representative images were chosen from *n* > 20 cells imaged per condition. (H) pHrodo-conjugated TfR bispecifics and control IgG were assayed for their relative effects on TfR levels after a 24-h incubation at 1 µM (gel image is representative of three samples). A reduction in TfR was observed for pHrodo–anti-TfR^A bispecific but not pHrodo–anti-TfR^D bispecific or control IgG. Bars, 10 µm.

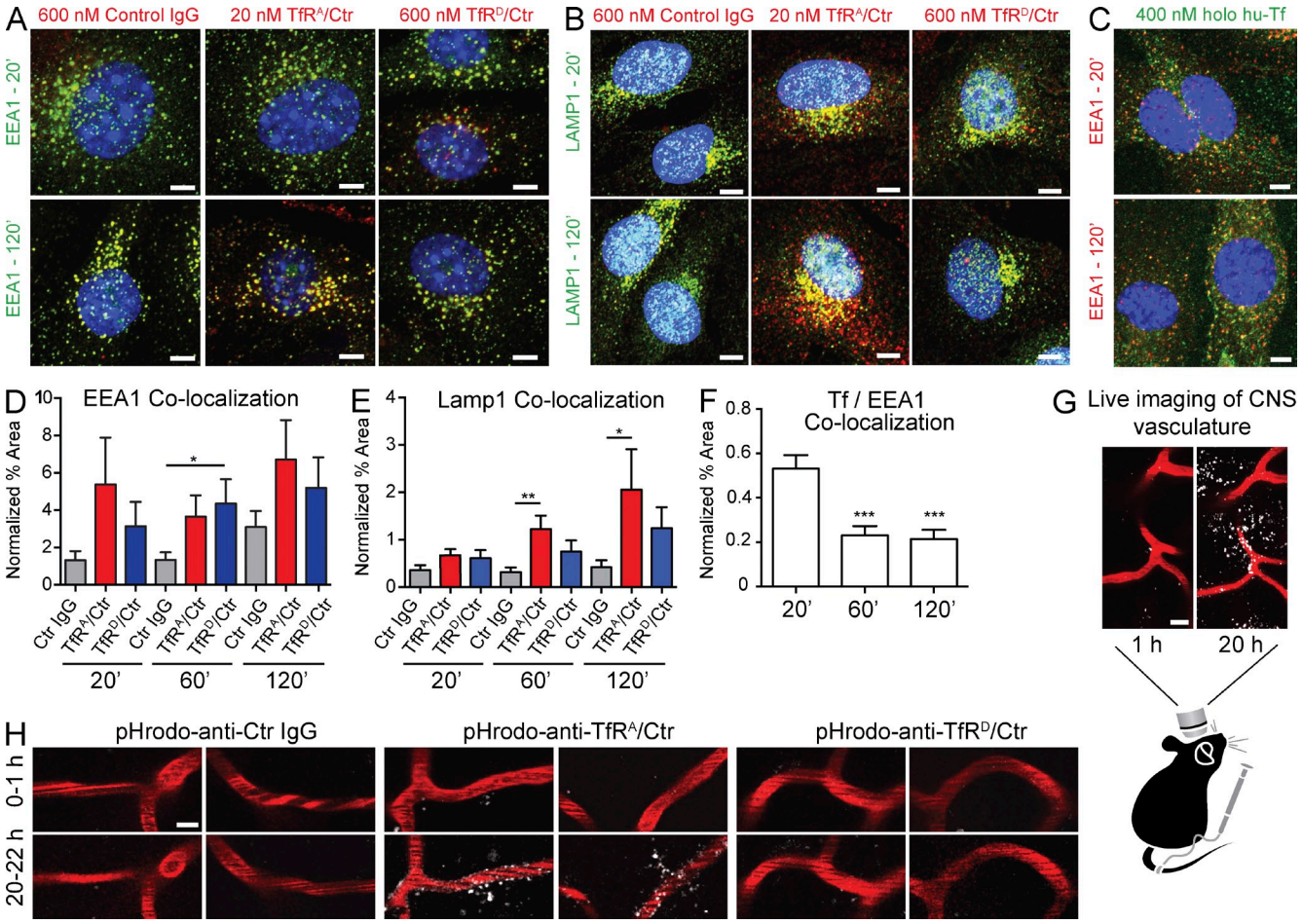

Figure 5. High-affinity anti-TfR colocalizes with lysosomes. (A and D) bEND.3 cells were incubated with 600 nM control IgG, 20 nM anti-TfR^A/control (Ctr), or 600 nM anti-TfR^D/control for 20, 60, and 120 min. The cells were fixed and immunostained for EEA1 and for the incubated antibodies with Alexa Fluor 594 anti–human IgG (red) and quantified for relative colocalized percent areas. (A) Representative confocal images of 20- and 120-min antibody incubations. (D) Quantification of colocalized percent area detected with EEA1 and anti–human IgG normalized to total percent area detected by anti-EEA1. (B) Representative images of anti-Lamp1 and control IgG, anti-TfR^A/control, or anti-TfR^D/control (at their respective IC_{50} concentrations) at 20 and 120 min. (E) Quantification for colocalized percent area for LAMP1 and each incubated antibody at the indicated time points normalized to LAMP1 total percent area. (C) bEND.3 cells were incubated with Alexa Fluor 488–labeled human holo-Tf (hu-Tf) at 400 nM for 20, 60, and 120 min and subsequently fixed and stained for EEA1. (F) Quantification of colocalized percent area detected with anti-EEA1 and Tf-488 and normalized to total percent area detected by EEA1. All bispecific antibody and Tf incubations were performed at 37°C. Data shown are the means ± SEM of $n = 3$ independent experimental repeats; within each experiment four fields were quantified from 100× confocal images of single optical z-planes. P-values were obtained by Student's *t* test versus control IgG (D and E) or versus 20-min time point (F): *, $P < 0.05$; **, $P \leq 0.01$; ***, $P \leq 0.001$. (G and H) In vivo imaging of cortical blood vessels labeled with AngioSense vascular dye (red) 1 and 20 h after i.v. injections with 10 mg/kg pHrodo–anti-TfR^A/control, pHrodo–anti-TfR^D/control, or pHrodo–control IgG. Punctate labeling of acidic compartments (white) is shown. Representative images from two different mice are shown for each antibody condition; $n = 2$ mice imaged per condition, with three to four imaging fields per mouse. Bars: (A–C and H) 5 µm; (G) 10 µm.

on the brain endothelial cell surface. Thus, we hypothesized that any reductions in receptor levels would significantly decrease anti-TfR brain exposure. To test this, we dosed mice with control IgG, TfR^A bispecific, or TfR^D bispecific at 50 mg/kg. After 48 h, all mice received anti-TfR^D/BACE1 bispecific at 50 mg/kg (except negative controls, which received an additional dose of control IgG). 1 d later, we assessed cortical TfR levels and antibody levels in brain and plasma to determine the relationship between TfR reductions and brain antibody uptake (Fig. 6 A), predicting that reduced TfR levels would lower the capacity for brain uptake. We measured total human IgG levels (combination of both doses) and specifically assessed the extent of transcytosis of anti-TfR^D/BACE1 (second dose) using a BACE1 capture ELISA, thereby allowing us to determine the impact on BBB transcytosis from TfR degradation caused by the initial injection with TfR^A bispecific.

The relative levels of TfR in the cortex of mice receiving TfR^A bispecific 1 d after the second injection (or on day 4 of the experiment) were decreased by 46%, compared with those receiving control IgG (Fig. 6, A and B). Mice receiving TfR^D bispecific showed a modest decrease in this experiment (28%), which likely reflects the effects of a high dose of total TfR^D

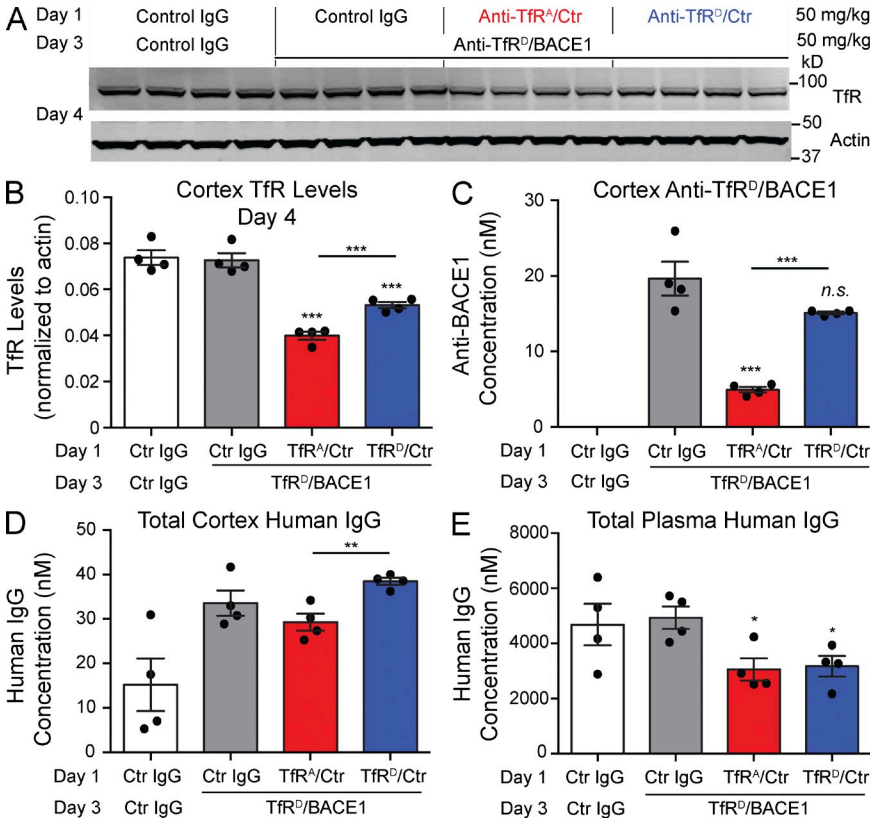

Figure 6. Degradation of TfR reduces BBB transcytosis capacity for a therapeutic bispecific antibody. (A) Multidose in vivo study paradigm to assess the effect of TfR degradation on BBB antibody transcytosis and Western blot analysis of cortical lysates. Mice were dosed i.v. with antibody at 50 mg/kg on day 1. After 48 h (day 3), each received either a control IgG or anti-TfR^D/BACE1 at 50 mg/kg. Each lane represents one individual mouse brain sample; $n = 4$ mice per group. (B) Brains were collected on day 4, and cortical lysates were probed by Western blot and quantified for TfR and actin levels. (C) Levels of anti-TfR^D/BACE1 on day 4 were determined by a BACE1-specific ectodomain capture ELISA. (D and E) Levels of total human IgG antibody concentrations in brain (D) and plasma (E) were determined by a generic human Fc ELISA. Bars represent mean ± SEM; p-values were obtained by Student's *t* test versus control IgG groups or as indicated: *, $P < 0.05$; **, $P \leq 0.01$; ***, $P \leq 0.001$. Ctr, control.

bispecific (Fig. 6, B and D), equaling 100 mg/kg over 3 d. Importantly, anti-TfR^D/BACE1 cortical concentrations were significantly lower in mice that initially received TfR^A bispecific, compared with mice dosed initially with either control IgG or TfR^D bispecific (Fig. 6 C). In contrast to the 75% reduction in brain uptake capacity with initial dosing of anti-TfR^A bispecific, mice initially dosed with anti-TfR^D bispecific had a minor decrease in anti-TfR^D/BACE1 compared with control IgG mice that was not statistically significant ($P = 0.09$) but may reflect the modest decrease observed in TfR levels (Fig. 6 B). Notably, TfR^A bispecific decreased brain TfR levels by 46% (Fig. 6 B), yet we observed a greater reduction in anti-TfR^D/BACE1 brain concentrations. We speculate that minimal remaining TfR^A bispecific may be competing with anti-TfR^D/BACE1 for TfR binding, contributing to the further reductions in cortical anti-TfR^D/BACE1 (Fig. 6 C). Total plasma antibody levels (from a combination of both doses) were not significantly different, and both were reduced compared with control IgG as the result of TfR-mediated clearance (Fig. 6 E). Thus, despite similar amounts of circulating plasma antibody concentrations between the two dosing groups (Fig. 6 E), mice with an initial anti-TfR^D/control dose had more total brain antibody levels than mice with an initial anti-TfR^A/control dose (Fig. 6 D). These results demonstrate that dosing with low-affinity antibodies against TfR effectively limits receptor degradation, thus maintaining its transport capacity and maximizing brain exposure.

DISCUSSION

We have previously shown that TfR bispecific antibodies cross the BBB and gain access to the brain and that reducing antibody affinity enhances brain exposure (Yu et al., 2011; Couch et al., 2013). Here we provide a cellular understanding of the relationship between TfR binding and TfR trafficking (Fig. 2 A) by demonstrating that high-affinity TfR antibody binding alters the intracellular trafficking fate of TfR and impacts its transcytosis capacity at the BBB. Using high and low TfR bispecific affinity variants, we showed that mice dosed with high-affinity TfR bispecific had reduced brain TfR levels. Furthermore, indium labeling of TfR antibodies revealed increased degradation of TfR^A bispecific in the brain. Collectively, our data show that high-affinity binding promotes both TfR and TfR antibody degradation. We hypothesized that high-affinity anti-TfR bispecifics alter TfR trafficking. Using a cellular model, we found that TfR^A bispecific actively drives TfR to lysosomes for degradation. To determine whether our cellular observations are relevant in vivo, we conducted live imaging with a pH-sensitive dye (pHrodo) conjugated to anti-TfR and observed similar lysosomal localization patterns in the brains of living mice, with high-affinity anti-TfR showing the most robust signal, including localization to both vasculature and presumably neurons. Ultimately, we found that decreased brain TfR caused by high-affinity TfR antibody could impair BBB transcytosis capacity and significantly reduce brain uptake of anti-TfR bispecific.

Because the complexity of an intact BBB within a neurovascular unit is difficult to model in a transwell culture of one or two cell types, the value of in vitro BBB systems for the study of complex physiological barrier functions is limited. Thus, we restricted our BBB transcytosis analyses to in vivo experimental paradigms, while using cellular assays with bEND.3 cells, which faithfully recapitulate TfR^{A} bispecific–induced TfR degradation to a similar extent as in vivo dosing, to understand trafficking alterations induced by TfR antibodies. Our combined findings reveal a fundamental cellular principle with translational implications, namely that TfR cellular trafficking is modulated by TfR antibody affinity. The TfR antibodies used in these experiments share an identical epitope and do not compete for Tf binding to TfR; furthermore, affinity differences are caused by single alanine substitutions. Whether TfR antibodies directed at other epitopes may also modulate degradation is unknown, but is under investigation. Importantly, current therapeutic strategies targeting TfR with high-affinity antibodies using chronic dosing paradigms may be severely hindered by the gradual loss of TfR, resulting in limited brain antibody uptake and also impacting physiological iron transport into the brain.

MATERIALS AND METHODS

Antibodies. All bispecific anti-TfR affinity variants used in this study were produced and assembled in-house (Genentech). Mouse-specific anti-TfR and anti-BACE1 contain mouse variable domains and human IgG backbones with mutations introduced in the Fc region that are required for Fcγ receptor binding, rendering them effectorless (Couch et al., 2013). Human anti–glycoprotein D was the isotype control IgG. Anti-TfR affinities have been previously determined as IC_{50} = 18 nM for anti-TfR^{A}/BACE1 and 588 nM for anti-TfR^{D}/BACE1 for monovalent binding to immobilized mouse antigen (Couch et al., 2013). Anti-TfR Fab fragment and QD conjugation was performed as described previously (Chung et al., 2010). Anti-TfR Fab used in QD conjugation and TIRFM experiments was digested from an in-house anti-TfR recognizing the Tf binding epitope of murine TfR (clone C12). pHrodo dye conjugation of anti-TfR bispecifics was performed according to vendor protocols (Life Technologies). LysoTracker Green DND-26 and Alexa Fluor 488–labeled human holo-Tf were obtained from Life Technologies.

Primary antibodies used for Western blot or immunostaining were mouse anti-TfR (1:2,000; clone H68.4; Life Technologies), rabbit anti-TfR (1:300; Abcam), rabbit anti-actin (1:4,000; Abcam), rabbit anti-EEA1 (1:400; Cell Signaling Technology), and rabbit anti-Lamp1 (1:2,000; Sigma-Aldrich). Secondary antibodies used for quantitative Western blot analyses were donkey anti–mouse and donkey anti–rabbit IgG conjugated to 800- or 680-nm fluorophores, respectively (1:2,000; LI-COR Biosciences). Alexa Fluor 594 anti–human and Alexa Fluor 488 anti–rabbit were used for immunocytochemistry detection (1:800; Life Technologies).

Animal experiments. Animal care and usage were performed under the guidelines provided by the Genentech Institutional Animal Care and Use Committee. Female wild-type C57BL/6 mice aged 6–8 wk were obtained from Charles River and/or the Jackson Laboratory unless otherwise indicated. Tail vein injections were administered at the indicated doses using a maximal volume of 200 µl (dilutions made in sterile PBS). The animals were randomly assigned into treatment groups but were not blind-coded during dosing, sample collection, or Western blot and ELISA analysis. After the specified time points, mice were anesthetized with Avertin, and plasma was collected for antibody ELISA assays (~500 µl) and transcardially perfused with ice-cold PBS at a rate of 2 ml/min for 8 min. Brains were subsequently harvested, split into halves, and dissected to isolate the cortices for assessment of antibody levels by ELISA and TfR levels by Western blot. Cortices were snap-frozen on dry ice until further processing.

Tissue processing. Frozen cortices were allowed to thaw slowly on wet ice. For antibody concentration assays and Western blot, cortices were homogenized using the TissueLyser (QIAGEN) in 1% NP-40/PBS supplemented with Complete Mini EDTA-free protease inhibitor cocktail (Roche). Homogenates were allowed to rotate for 1 h at 4°C and subsequently spun at 14,000 rpm for 20 min at 4°C, and the supernatant was removed and aliquoted for protein concentration determination by a BCA assay (Thermo Fisher Scientific).

Immunohistochemistry and quantitative analysis. Mice injected with 50 mg/kg TfR bispecific were PBS perfused 4 d after dosing, and brains were harvested and drop fixed in 4% paraformaldehyde for 48 h (n = 4 mice per antibody treatment group). Serial sagittal sections were collected on a freezing stage sliding microtome at 30 µm (Leica). Every eighth section (spaced 240 µm apart) was immunostained with rabbit anti-TfR (Abcam), Alexa Fluor 488 donkey anti–rabbit IgG, and Alexa Fluor 594 goat anti–human IgG to visualize the injected antibodies. Images of hippocampus from three adjacent sections were acquired at room temperature with a 20× objective on a DM550B epifluorescent microscope (Leica) equipped with a DFC360 camera (Leica) running LAS software (Leica). Acquisition parameters were identical for all samples, and images were quantified using ImageJ software (National Institutes of Health) as described previously (Bien-Ly et al., 2012). Slides were blind-coded during image acquisition and analysis.

ELISA for plasma and brain antibody concentrations. Whole blood was collected before perfusion and spun in Microtainer tubes containing EDTA (BD) at 5,000 *g* for 90 s. The supernatant was removed and snap frozen before all assays. Antibody concentrations were measured by ELISA as previously described (Atwal et al., 2011). In brief, the human IgG Fc ELISA uses F(ab′)2 donkey anti–human IgG, Fc fragment–specific polyclonal antibody (Jackson ImmunoResearch Laboratories, Inc.) as the coat and horseradish peroxidase–conjugated F(ab′)2 goat anti–human IgG, Fc fragment–specific polyclonal antibody (Jackson ImmunoResearch Laboratories, Inc.) as the detection antibody. The anti-BACE1–specific ELISA uses recombinant BACE1 ectodomain as the coating antigen and the same detection antibody as in the human IgG Fc ELISA. Injected antibodies were used as internal control standards (anti–control IgG, anti-TfR/BACE1 variants, and anti-TfR/control IgG variants) to quantify the respective antibody concentrations.

DOTA conjugation and ^{111}Indium incorporation. Aliquots containing 5 mg anti-TfR^{A}/control IgG, anti-TfR^{D}/control IgG, and the IgG1 control antibody (Genentech) were exchanged from their respective formulation buffers (proprietary) into aqueous 50 mM sodium borate, pH 8.5, using Illustra NAP5 columns (GE Healthcare). Exactly 5 molar equivalents of the *N*-hydroxysuccinimidyl ester of 1,4,7,10-tetraazacyclododecane-*N*,*N*′,*N*″,*N*‴-tetraacetic acid (DOTA-NHS) in 0.68 µl dimethylformamide was added to 600 µl sodium borate–buffered (pH 8.5) antibody solutions. Reaction mixtures were gently agitated for 1 h at 37°C. The reaction was terminated by promptly applying the mixtures to NAP5 columns preequilibrated in aqueous 0.3 M ammonium acetate buffer, pH 7.0.

^{111}Indium was incorporated into DOTA through the addition of a 3-µl (820 µCi) aliquot of ^{111}In[Cl] (MDS Nordion) to a 17-µl aliquot of the ammonium acetate–buffered DOTA-conjugated antibodies. Reaction mixtures were gently agitated for 1 h at 37°C. A 5-µl aliquot of 50 mM aqueous EDTA challenge solution was added, followed by an additional 75-µl aliquot of aqueous 0.3 M ammonium acetate buffer, pH 7.0. The mixture was applied to a NAP5 column, from which the radiolabeled protein eluted in a 500-µl fraction of PBS. Purity was assessed by size-exclusion HPLC.

Radioiodination. Anti-TfR^{A}/control IgG, anti-TfR^{D}/control IgG, and the IgG1 control antibody were radioiodinated with iodine-125 (^{125}I) using the indirect iodogen addition method as previously described (Chizzonite et al., 1991). The radiolabeled proteins were purified using NAP5 columns preequilibrated in PBS. Purity was assessed by size-exclusion HPLC.

In vivo biodistribution in C57BL/6 female mice. Female C57BL/6 mice of ~6–8 wk of age were obtained from Charles River. They were

co-administered with 5 µCi each of radioiodinated and DOTA-radioindium–labeled anti-TfR^A/control IgG (0.025 mg/kg), anti-TfR^D/control IgG (0.021 mg/kg), or control IgG (0.020 mg/kg) via tail vein i.v. bolus. At 1, 4, 24, and 96 h after dose, blood (processed for plasma), brain, liver, spleen, bone marrow, and muscle (gastrocnemius) were collected ($n = 3$) and stored frozen until analyzed for total radioactivity on a gamma counter (2480 Wizard² Automatic Gamma Counter; PerkinElmer). The radioactivity level in each sample was calculated and expressed as percentage of injected dose (ID) per gram or milliliter of sample (%ID/g or %ID/ml). The percentage degraded in each tissue was calculated by subtracting the %ID from the ^{125}I signal from that of ^{111}In. This is based on the assumption that ^{125}I clears from cells after intracellular antibody degradation and its signal represents intact antibody, whereas ^{111}In catabolites accumulate in cells as a result of the residualizing properties of the charged and highly polar DOTA chelator, and its signal therefore represents intact and degraded antibody (Boswell et al., 2012). The levels of ^{111}In and ^{125}I radioactivity in spleen and bone marrow were similar to brain as the result of affinity-driven uptake. Liver and muscle displayed nonspecific uptake with similar signals arising from all three radiolabeled antibodies for both ^{111}In and ^{125}I.

Cell culture, Western blotting, immunoprecipitation, and immunocytochemistry. bEND.3 cells were obtained from the ATCC (CRL-2299) and passaged once to generate low-passage stocks, each of which was used in experiments until passage 36. Cells were maintained at 37°C, 5% CO_2, in high-glucose DMEM supplemented with 1% L-glutamine, 1% penicillin/streptomycin, and 10% fetal bovine serum and passaged twice weekly with 0.5% trypsin. Antibodies and bafilomycin A1 (Santa Cruz Biotechnology, Inc.) were diluted in growth media and incubated with the cells for the time intervals as stated. Before harvesting the cells by scraping, the cells were washed three times in ice-cold PBS and lysed in RIPA buffer (25 mM Tris-HCl, 150 mM NaCl, 1% NP-40, 1% sodium deoxycholate, and 0.1% SDS) with protease inhibitors. Protein concentration in cell lysates was determined using BCA (Thermo Fisher Scientific) before Western blotting, and 15 µg of protein was loaded onto 4–12% Bis-Tris Novex gels (Life Technologies). Gels were transferred onto nitrocellulose membranes using the iBlot system (Life Technologies), and Western blotting was performed using Odyssey blocking buffer reagents and secondary antibodies (LI-COR Biosciences). Western blot membranes were imaged and quantified using manufacturer-supplied software and system (Odyssey; LI-COR Biosciences).

Cells incubated with anti-TfR bispecifics or Alexa Fluor 488 human holo-Tf for immunocytochemistry and colocalization analyses were grown on glass chamber slides (BD) coated with rat tail collagen I (BD) and were randomly assigned treatment groups within each independent experiment. After 1-h incubation at 37°C, the cells were washed three times in ice cold PBS, fixed immediately thereafter with 4% PFA for 15 min at 4°C, and subsequently rinsed three times in PBS. The cells were then permeabilized in 0.1% Triton X-100 for 10 min, blocked for 1 h in 5% BSA/PBS, and incubated with primary antibodies overnight in blocking buffer. Detection followed with Alexa Fluor–labeled secondary antibodies and coverslips were applied using Prolong Anti-Fade Gold with DAPI (Life Technologies). Slides were randomly blind-coded as to antibody treatment and time point during all image acquisition and colocalization analyses.

Confocal imaging and colocalization analysis. Images of EEA1- and LAMP1-stained cells were acquired at room temperature with an LSM780 confocal microscope operating ZEN software version 2010 (Carl Zeiss). A 100× oil objective was used to capture all images with a digital zoom factor of 2–4×. All imaging parameters remained constant (pinhole, power, and gain) for each set of slides imaged for a particular subcellular marker and within each independent experiment because of differences in signal intensity for EEA1 or Lamp1 and across experiments. One optical z plane was captured for four fields per condition (each field typically containing four to six cells) and was quantified for percent area colocalized between the red and green channels (antibody and marker, respectively) using the ZEN software colocalization analysis suite. Intensity thresholds were determined within each experiment for colocalization analyses and quantification of signal intensities; these values varied between experiments. The colocalized relative area of incubated antibody was normalized to LAMP1 or EEA1 relative area to control for signal intensity differences within experiments. Therefore, the "normalized % area" does not represent the fraction of colocalized antibody with LAMP1 to LAMP1 relative area because quantified colocalized relative areas were at times larger than LAMP1 areas. We assumed that the amounts of internalized antibody were similar among the bispecifics because they were incubated at their IC_{50} concentrations. The experiment was repeated independently three times, and the results of each were averaged to obtain final means ± SEM.

TIRFM imaging system and analysis. Imaging was performed on an Eclipse TE2000 inverted microscope (Nikon) with 100×/1.49 NA Plan Apochromat objectives (Nikon) with bEND.3 cells grown on 35-mm glass bottom dishes (MatTek) coated with rat tail collagen I. Cells were allowed to reach at least 70% confluency before incubation with antibodies for live imaging experiments. Illumination of samples was by the 488- and 568-nm line of a solid-state laser, and images were captured by the iXon back-illuminated EMCCD camera (Andor Technology). Surface movement of TfR Fab:QD was tracked and quantified with an ImageJ plug-in and Imaris (Bitplane).

Quantitative PCR. RNA from bEND.3 cells treated with anti-TfR bispecifics was isolated using the RNeasy Plus Micro kit (QIAGEN). FAM-labeled mouse TfR and VIC-labeled mouse β-actin TaqMan probe sets were obtained from Life Technologies. Quantitative PCR reagents were obtained from the Path-ID Multiplex One-Step RT-PCR kit (Life Technologies), and the assay was run on a 7500 series Real-Time PCR system (Applied Biosystems).

In vivo two-photon microscopy. 8–16-wk-old female Cx3cr1-GFP mice were implanted with cranial windows above the somatosensory cortex, as previously described (Holtmaat et al., 2009), and imaged 1.5–2 wk after surgeries. Immediately before imaging, mice were anesthetized with isoflurane (1.5%, 1 liter/min) and injected with 100 µl AngioSense 680 (VisEn Medical) via a lateral tail vein catheter to visualize vasculature and 10 mg/kg pHrodo-labeled TfR bispecifics. Pilot experiments established that no pHrodo signal was detectable within the first 2 h after injection. Anesthetized mice were mounted to the microscope via a head post. The two-photon laser-scanning microscope system (Ultima In Vivo Multiphoton Microscopy System; Prairie Technologies) uses a Ti:sapphire laser (MaiTai DeepSee Spectra Physics) tuned to 860 nm delivering ∼15 mW to the back-focal plane of a 60× objective. Laser power was kept constant across imaging days for each animal. Three to four 100 × 100–µm field of views were imaged <1 h after injection for each animal and again 20–22 h later.

Statistical analysis. All values are expressed as mean ± SEM, and p-values were assessed by unpaired, two-tailed, Student's t test, unless otherwise indicated. $P < 0.05$ was considered statistically significant. Exact n numbers are listed in figure legends or shown by scatter points. Correlation analysis between brain TfR and antibody levels and was performed using Prism version 6 (GraphPad Software).

We thank A. Bruce for graphics, R. Tong and J. Ernst for the generation of bispecific antibodies, X. Chen and Y. Chen for generation of C12 anti-TfR, S. Lee for TfR Fab generation and labeling, L. Khawli and S. Ulufato for input and assistance with trace uptake studies, and G. Ayalon and D. Hansen for critical comments.

All authors are paid employees of Genentech Inc. The authors declare no further competing financial interests.

Submitted: 6 August 2013
Accepted: 10 January 2014

REFERENCES

Atwal, J.K., Y. Chen, C. Chiu, D.L. Mortensen, W.J. Meilandt, Y. Liu, C.E. Heise, K. Hoyte, W. Luk, Y. Lu, et al. 2011. A therapeutic antibody targeting BACE1 inhibits amyloid-β production in vivo. *Sci. Transl. Med.* 3:84ra43. http://dx.doi.org/10.1126/scitranslmed.3002254

Bien-Ly, N., A.K. Gillespie, D. Walker, S.Y. Yoon, and Y. Huang. 2012. Reducing human apolipoprotein E levels attenuates age-dependent Aβ accumulation

in mutant human amyloid precursor protein transgenic mice. *J. Neurosci.* 32:4803–4811. http://dx.doi.org/10.1523/JNEUROSCI.0033-12.2012

Boswell, C.A., D. Bumbaca, P.J. Fielder, and L.A. Khawli. 2012. Compartmental tissue distribution of antibody therapeutics: experimental approaches and interpretations. *AAPS J.* 14:612–618. http://dx.doi.org/10.1208/s12248-012-9374-1

Chizzonite, R., T. Truitt, F.J. Podlaski, A.G. Wolitzky, P.M. Quinn, P. Nunes, A.S. Stern, and M.K. Gately. 1991. IL-12: monoclonal antibodies specific for the 40-kDa subunit block receptor binding and biologic activity on activated human lymphoblasts. *J. Immunol.* 147:1548–1556.

Chung, I., R. Akita, R. Vandlen, D. Toomre, J. Schlessinger, and I. Mellman. 2010. Spatial control of EGF receptor activation by reversible dimerization on living cells. *Nature*. 464:783–787. http://dx.doi.org/10.1038/nature08827

Couch, J.A., Y.J. Yu, Y. Zhang, J.M. Tarrant, R.N. Fuji, W.J. Meilandt, H. Solanoy, R.K. Tong, K. Hoyte, W. Luk, et al. 2013. Addressing safety liabilities of TfR bispecific antibodies that cross the blood-brain barrier. *Sci. Transl. Med.* 5:183ra57. http://dx.doi.org/10.1126/scitranslmed.3005338

Dautry-Varsat, A., A. Ciechanover, and H.F. Lodish. 1983. pH and the recycling of transferrin during receptor-mediated endocytosis. *Proc. Natl. Acad. Sci. USA*. 80:2258–2262. http://dx.doi.org/10.1073/pnas.80.8.2258

Dufès, C., M. Al Robaian, and S. Somani. 2013. Transferrin and the transferrin receptor for the targeted delivery of therapeutic agents to the brain and cancer cells. *Ther. Deliv.* 4:629–640. http://dx.doi.org/10.4155/tde.13.21

Fishman, J.B., J.B. Rubin, J.V. Handrahan, J.R. Connor, and R.E. Fine. 1987. Receptor-mediated transcytosis of transferrin across the blood-brain barrier. *J. Neurosci. Res.* 18:299–304. http://dx.doi.org/10.1002/jnr.490180206

Gosk, S., C. Vermehren, G. Storm, and T. Moos. 2004. Targeting anti-transferrin receptor antibody (OX26) and OX26-conjugated liposomes to brain capillary endothelial cells using in situ perfusion. *J. Cereb. Blood Flow Metab.* 24:1193–1204. http://dx.doi.org/10.1097/01.WCB.0000135592.28823.47

Holtmaat, A., T. Bonhoeffer, D.K. Chow, J. Chuckowree, V. De Paola, S.B. Hofer, M. Hübener, T. Keck, G. Knott, W.C. Lee, et al. 2009. Long-term, high-resolution imaging in the mouse neocortex through a chronic cranial window. *Nat. Protoc.* 4:1128–1144. http://dx.doi.org/10.1038/nprot.2009.89

Jefferies, W.A., M.R. Brandon, S.V. Hunt, A.F. Williams, K.C. Gatter, and D.Y. Mason. 1984. Transferrin receptor on endothelium of brain capillaries. *Nature*. 312:162–163. http://dx.doi.org/10.1038/312162a0

Jones, A.R., and E.V. Shusta. 2007. Blood-brain barrier transport of therapeutics via receptor-mediation. *Pharm. Res.* 24:1759–1771. http://dx.doi.org/10.1007/s11095-007-9379-0

Kissel, K., S. Hamm, M. Schulz, A. Vecchi, C. Garlanda, and B. Engelhardt. 1998. Immunohistochemical localization of the murine transferrin receptor (TfR) on blood-tissue barriers using a novel anti-TfR monoclonal antibody. *Histochem. Cell Biol.* 110:63–72. http://dx.doi.org/10.1007/s004180050266

Manich, G., I. Cabezón, J. del Valle, J. Duran-Vilaregut, A. Camins, M. Pallàs, C. Pelegrí, and J. Vilaplana. 2013. Study of the transcytosis of an anti-transferrin receptor antibody with a Fab' cargo across the blood-brain barrier in mice. *Eur. J. Pharm. Sci.* 49:556–564. http://dx.doi.org/10.1016/j.ejps.2013.05.027

Matsui, T., T. Itoh, and M. Fukuda. 2011. Small GTPase Rab12 regulates constitutive degradation of transferrin receptor. *Traffic*. 12:1432–1443. http://dx.doi.org/10.1111/j.1600-0854.2011.01240.x

Moos, T., and E.H. Morgan. 2001. Restricted transport of anti-transferrin receptor antibody (OX26) through the blood-brain barrier in the rat. *J. Neurochem.* 79:119–129. http://dx.doi.org/10.1046/j.1471-4159.2001.00541.x

Paris-Robidas, S., V. Emond, C. Tremblay, D. Soulet, and F. Calon. 2011. In vivo labeling of brain capillary endothelial cells after intravenous injection of monoclonal antibodies targeting the transferrin receptor. *Mol. Pharmacol.* 80:32–39. http://dx.doi.org/10.1124/mol.111.071027

Predescu, S.A., D.N. Predescu, and A.B. Malik. 2007. Molecular determinants of endothelial transcytosis and their role in endothelial permeability. *Am. J. Physiol. Lung Cell. Mol. Physiol.* 293:L823–L842. http://dx.doi.org/10.1152/ajplung.00436.2006

Roberts, R.L., R.E. Fine, and A. Sandra. 1993. Receptor-mediated endocytosis of transferrin at the blood-brain barrier. *J. Cell Sci.* 104:521–532.

Rubin, L.L., and J.M. Staddon. 1999. The cell biology of the blood-brain barrier. *Annu. Rev. Neurosci.* 22:11–28. http://dx.doi.org/10.1146/annurev.neuro.22.1.11

Sheff, D., L. Pelletier, C.B. O'Connell, G. Warren, and I. Mellman. 2002. Transferrin receptor recycling in the absence of perinuclear recycling endosomes. *J. Cell Biol.* 156:797–804. http://dx.doi.org/10.1083/jcb.20111048

Traer, C.J., A.C. Rutherford, K.J. Palmer, T. Wassmer, J. Oakley, N. Attar, J.G. Carlton, J. Kremerskothen, D.J. Stephens, and P.J. Cullen. 2007. SNX4 coordinates endosomal sorting of TfnR with dynein-mediated transport into the endocytic recycling compartment. *Nat. Cell Biol.* 9:1370–1380. http://dx.doi.org/10.1038/ncb1656

Yu, Y.J., and R.J. Watts. 2013. Developing therapeutic antibodies for neurodegenerative disease. *Neurotherapeutics*. 10:459–472. http://dx.doi.org/10.1007/s13311-013-0187-4

Yu, Y.J., Y. Zhang, M. Kenrick, K. Hoyte, W. Luk, Y. Lu, J. Atwal, J.M. Elliott, S. Prabhu, R.J. Watts, and M.S. Dennis. 2011. Boosting brain uptake of a therapeutic antibody by reducing its affinity for a transcytosis target. *Sci. Transl. Med.* 3:84ra44. http://dx.doi.org/10.1126/scitranslmed.3002230